Impact of Oxygen-Vacancies on Electrical Conductivity and Electrocatalytic Activity of $La_{3-x}Ca_xFe_2GaO_{9-\delta}$ (x = 0, 2; δ = 0, 1)

Kinithi M. K. Wickramaratne[a], Farshid Ramezanipour[a,*]

[a]Department of Chemistry, University of Louisville, Louisville, Kentucky 40292, USA

Abstract

The effect of oxygen-vacancies on functional properties is demonstrated through the investigation of $LaCa_2Fe_2GaO_8$, which has a perovskite-related structure, where oxygen-vacancies appear in every third layer, converting the octahedral coordination into tetrahedral. This effect is highlighted when the properties of this material are compared to that of $La_3Fe_2GaO_9$ ($LaFe_{0.67}Ga_{0.33}O_3$), which has the same Fe/Ga stoichiometry but lacks oxygen-vacancies. Since the electrocatalytically active metals in $ABO_{3-\delta}$ catalysts are the transition metals, the role of the A-site metals (La and Ca) is to modify the structural features of the material. While the electrocatalytic performance of these systems is lower than that of the state of the art catalysts, they show an excellent example of structure-activity relationships. The vacancy-ordered $LaCa_2Fe_2GaO_8$ shows better HER electrocatalytic performance compared to $La_3Fe_2GaO_9$. The former also shows a faster HER kinetics. We have also studied the electrical conductivity in a wide range of temperatures, indicating the enhanced electrical charge-transport properties of $LaCa_2Fe_2GaO_8$. Therefore, both electrical conductivity and HER electrocatalysis are improved due to the ordered arrangement of oxygen-vacancies in $LaCa_2Fe_2GaO_8$ as compared to $La_3Fe_2GaO_9$.

Keywords: Hydrogen-evolution reaction, Oxygen-vacancies, Perovskite Oxide, Structure-activity relationships, Water splitting,

1. INTRODUCTION

Hydrogen molecule is an excellent energy carrier and is considered a promising alternative to traditional fossil fuels due to its high mass-energy density and clean combustion.[1-2] Among a variety of methods, electrochemical water splitting by a water electrolyzer is one of the most promising methods to convert water molecules into hydrogen and oxygen gas. [3-4] Hydrogen evolution reaction (HER) mechanism comprises adsorption and desorption processes, where each step requires a potential, depending on the strength of hydrogen adsorption and desorption on the catalyst's surface. [5-6] Therefore, the development of sustainable catalysts that can lower the overpotential of this reaction is important to facilitate the overall process. Pt and Ru/Ir-based materials have been widely used as electrocatalysts for this reaction, but the high cost of these materials has limited their use. [7-8]

Different oxides, such as perovskite-related systems,[9-10] have been investigated as alternative catalysts. Among various families of perovskite oxides, oxygen-deficient perovskites ($ABO_{3-\delta}$) can be good candidates for this application due to their versatile structural, chemical, and physical properties. [11-14] Their properties can be modulated by changing the concentration and ordering of oxygen vacancies using different synthesis conditions or by substituting various metal cations.[15-16] The oxygen vacancies can have random or ordered arrangements within the structure.[17-18] The ability to modify the structures of these materials can lead to the development of high-performance electrocatalysts for water splitting.

One possible type of vacancy order is found in the $ABO_{2.67}$ ($A_3B_3O_8$) system, sometimes called the Greiner phase or bilayer brownmillerite. [19] In this structure, oxygen vacancies are present in every third layer, transforming the 6-coordinated geometry into 4-coordinated.[20] This results in a tetrahedral layer alternating with two octahedral layers.[19] This anion-vacancy ordered structure is

an intermediate between perovskite and brownmillerite.[4, 21] The structure can contain cooperative twisting of tetrahedral chains that determines the unit cell symmetry.[21-23] For instance, when right-handed and left-handed tetrahedral chains twist alternate between adjacent tetrahedral layers, the structure is described by the *Pbma* space group.[22] If all tetrahedral chains are twisted in the same direction, the structure crystallizes in $P2_1ma$,[23] and if the directions of the twist of different tetrahedral chains are disordered, the structure can be described by the *Pmma* space group.[21]

Our group has recently studied a wide range of oxide systems for electrocatalytic applications. [12, 15, 24-26] In the present work, we have shown the effect of oxygen vacancies and their ordering on electrocatalytic properties. We have synthesized $LaCa_2Fe_2GaO_8$ ($La_{0.33}Ca_{0.67}Fe_{0.67}Ga_{0.33}O_{2.67}$) with bilayer brownmillerite structure and have shown its enhanced properties compared to the analogous vacancy-free perovskite $La_3Fe_2GaO_9$ ($LaFe_{0.67}Ga_{0.33}O_3$). While the electrocatalytic performance of these materials is lower than those reported for the state of the art catalysts, these oxide systems show an excellent example of structure-activity relationships.

2. EXPERIMENTAL

Synthesis and Characterization. Samples of $LaCa_2Fe_2GaO_8$ and $La_3Fe_2GaO_9$ ($LaFe_{0.67}Ga_{0.33}O_3$) were synthesized under argon by the solid-state synthesis method. Suitable stoichiometric proportions of precursors, La_2O_3, $CaCO_3$, Fe_2O_3, and Ga_2O_3 were ground by agate mortar and pestle and pressed into pellets. The pellets were heated at 1250 ℃ for two periods of 48 hours under argon atmosphere. The structures of the obtained materials were studied by powder X-ray diffraction at room temperature using Cu Kα1 radiation (λ = 1.54056 Å). Rietveld refinements were done using GSAS program [27] and EXPIGU interface. [28] The oxygen contents were determined using iodometric titration [29], where 50 mg of the sample was dissolved in a 1 M HCl

solution containing an excess of KI (~2 g) under argon atmosphere. Then 5.0 mL of the solution was pipetted out for titration. The liberated I_2 was titrated with 0.025 M $Na_2S_2O_3$ solution. The starch solution was used as the indicator. A field emission scanning electron microscope was used to study the sample morphologies.

Electrochemical measurements. The catalyst ink for electrochemical measurements was prepared using 35 mg of the catalyst material, 7 mg of carbon black powder, 40 µL of Nafion D-521 solution (5% w/w in water and 1-propanol), and 7 mL of Tetrahydrofuran 99% (THF). Then, the mixture was ultrasonically dispersed in water for 15 minutes. Twenty microliters of the prepared catalyst ink were loaded onto the surface of a glassy carbon electrode (diameter = 5 mm, area = 0.196 cm^2) with a mass loading of 1.02 mg/cm^2 and dried overnight. Electrochemical measurements were done using a standard three-electrode electrochemical cell connected to a rotating disk electrode and a potentiostat. A commercial Ag/Agcl in 4 M KCl were used as reference electrode and carbon electrode as the counter electrode for electrochemical experiments. Electrical conductivities were measured using rectangular sintered pellets, sandwiched between gold leads. The electrical conductivity data were collected at a temperature range from 25 to 800 °C. The rates of heating and cooling for conductivity measurements were 3 °C/min.

3. RESULTS AND DISCUSSION

3.1. Crystal Structure

The Rietveld refinement profiles for both $LaCa_2Fe_2GaO_8$ ($La_{0.33}Ca_{0.67}Fe_{0.67}Ga_{0.33}O_{2.67}$) and $La_3Fe_2GaO_9$ ($LaFe_{0.67}Ga_{0.33}O_3$) using X-ray diffraction (XRD) data are shown in Figure 1. Also, the refined structural parameters are listed in Tables 1 and 2. The material without oxygen-vacancies, $La_3Fe_2GaO_9$ ($LaFe_{0.67}Ga_{0.33}O_3$), has a typical structure (Figure 2a) of an ABO_3 perovskite, with AO_{12} (A = La) and BO_6 (B = Fe, Ga) polyhedra. Here the B-site metals Fe/Ga have octahedral geometry whereas the A-site metal, La, occupies the spaces between those octahedra. The Fe-only compound, $LaFeO_3$,[30-31] and Ga-only compound, $LaGaO_3$,[32] are both known to crystalize in the *Pnma* space group. Therefore, the *Pnma* structure of $La_3Fe_2GaO_9$ ($LaFe_{0.67}Ga_{0.33}O_3$) was expected.

The incorporation of Ca^{2+}, which has a lower valance than La^{3+}, results in the transformation of the structure and the formation of an oxygen-deficient perovskite, $LaCa_2Fe_2GaO_8$ ($La_{0.33}Ca_{0.67}Fe_{0.67}Ga_{0.33}O_{2.67}$), with an ordered structure (Figure 2b). This material has a general formula $AA'_2B'B_2O_8$. Therefore, it contains four different metal sites with different coordination geometries, namely AO_{12} (A = La), $A'O_8$ (A' = Ca), $B'O_4$ (B' = Ga), and BO_6 (B=Fe). The refinement of Fe and Ga occupancies indicated that at room temperature Fe is almost entirely located on octahedral sites and Ga on tetrahedral sites. This is consistent with the smaller ionic radius of Ga^{3+} compared to Fe^{3+}.

Also, most of the La^{3+} cations are located on 12-coordinated A-sites which are in between the BO_6 octahedra. On the other hand, the Ca^{2+} cations are on the 8-coordinated A'-sites that reside between $B'O_4$ and BO_6 layers. Rietveld refinements confirm that $LaCa_2Fe_2GaO_8$ crystallizes in space groups *Pbma*, consistent with a previous report of the structure of this material. [22]

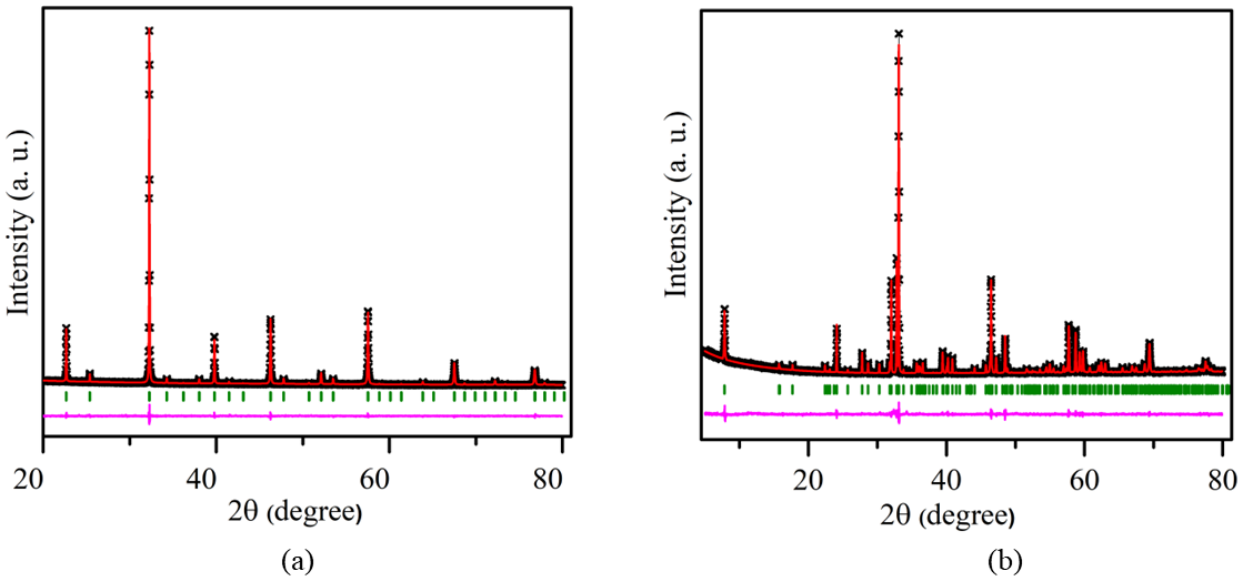

Figure 1. Rietveld refinement profiles of (a) $La_3Fe_2GaO_9$ ($LaFe_{0.67}Ga_{0.33}O_3$, *Pnma*) and (b) $LaCa_2Fe_2GaO_8$ (*Pbma*). The cross symbols, solid red line, olive vertical tick marks, and lower magenta line correspond to experimental data, the calculated pattern for the structural model, Bragg peak positions, and the difference plot, respectively.

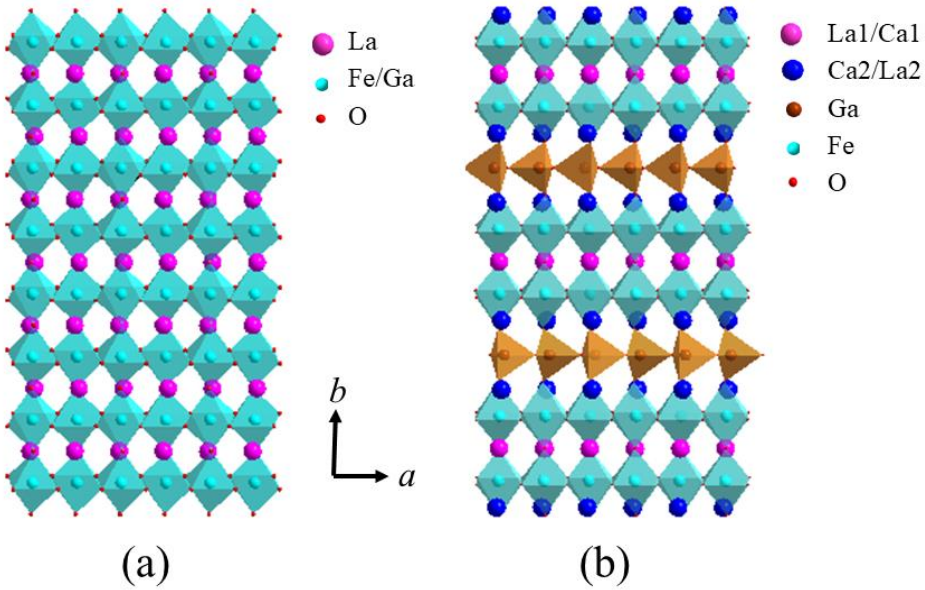

Figure 2. Crystal structures of (a) $La_3Fe_2GaO_9$ ($LaFe_{0.67}Ga_{0.33}O_3$) and (b) $LaCa_2Fe_2GaO_8$.

Table 1. Refined Structural Parameters for $LaFe_{0.67}Ga_{0.33}O_3$ at Room Temperature by using Powder X-ray Diffraction Data. Space Group: *Pnma*, *a* = 5.5463(1) Å, *b* = 7.8466(2) Å, *c* = 5.5438(8) Å, R_p = 0.0350, wR_p = 0.0446

Atom	x	y	z	Occupancy	Multiplicity	U_{iso} (Å^2)
La	0.02455(1)	0.25	-0.00257(1)	1	4	0.0215(4)
Fe	0.5	0	0	0.6667(0)	4	0.0249(6)
Ga	0.5	0	0	0.3333(0)	4	0.02487
O1	-0.014667(1)	0.25	0.438950(5)	1	4	0.0035(2)
O2	0.78204(2)	0.44738(1)	0.75575(3)	1	8	0.0035(2)

Table 2. Refined Structural Parameters for $La_{0.33}Ca_{0.67}Fe_{0.67}Ga_{0.33}O_{2.67}$ at Room Temperature by using Powder X-ray Diffraction Data. Space Group: *Pbma*, *a* = 5.4608(1) Å, *b* = 22.5120(3) Å, *c* = 5.5919(1) Å, R_p = 0.0198, wR_p = 0.0278.

Atom	x	y	Z	Occupancy	Multiplicity	U_{iso} (Å^2)
La1	0.25	0	0.7433(6)	0.89(1)	4	0.0608(1)
Ca1	0.25	0	0.7433(6)	0.12(1)	4	0.0608(1)
La2	0.27597(1)	0.15776(1)	0.72581(1)	0.08(1)	8	0.0600(3)
Ca2	0.27597(1)	0.15776(1)	0.72581(1)	0.92(1)	8	0.0500(3)
Ga1	0.30542(1)	0.25	0.1799(9)	1	4	0.0579(3)
Fe2	0.25715(1)	0.08656(3)	0.24170(1)	1	8	0.0578(2)
O1	0.25	0	0.175(5)	1	4	0.0681(3)
O2	0.656(4)	0.25	0.115(4)	1	4	0.0681(3)
O3	0.238(4)	0.1784(9)	0.33212(2)	1	8	0.0681(3)
O4	0.001(6)	0.0974(7)	0.97385(3)	1	8	0.0681(3)
O5	0.993(7)	0.0772(8)	0.498(4)	1	8	0.0681(3)

The Fe and Ga stoichiometries are the same in both materials. The regular perovskite $La_3Fe_2GaO_9$ ($LaFe_{0.67}Ga_{0.33}O_3$) was synthesized to allow a direct comparison with $LaCa_2Fe_2GaO_8$, in order to highlight the effect of oxygen vacancies on functional properties. We note that it is well established [9, 33] that catalytically active metals in oxide OER/HER catalysts are transition metals, and the A-site metals (La/Ca) do not directly participate in the catalytic process. [34-35] Here, the role of A-site metal is to modify the structural features of these materials.

The morphologies of sintered pellets were probed using scanning electron microscopy, and the results are shown in Figure 3. As seen here, the crystallites in $LaCa_2Fe_2GaO_8$ are much larger than those of $La_3Fe_2GaO_9$ ($LaFe_{0.67}Ga_{0.33}O_3$). The oxygen contents of the materials were confirmed by iodometric titrations. The results were consistent with formulas $LaCa_2Fe_2GaO_8$ and $La_3Fe_2GaO_9$ ($LaFe_{0.67}Ga_{0.33}O_3$).

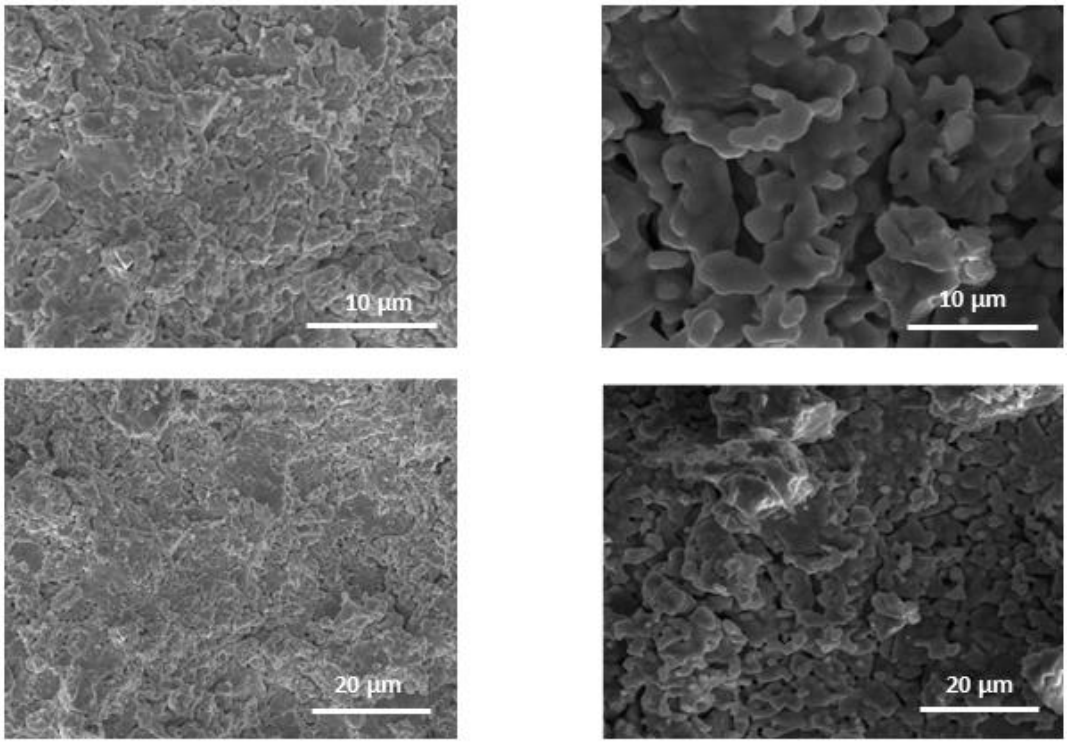

Figure 3. Scanning electron microscopy (SEM) images of (a) $La_3Fe_2GaO_9$ ($LaFe_{0.67}Ga_{0.33}O_3$) and (b) $LaCa_2Fe_2GaO_8$.

3.2. Electrical Conductivity

The electrical conductivity measurements were done in the temperature range of 25 ℃ to 800 ℃. The conductivity is related to resistance (R) through $\sigma = \frac{l}{RA}$, where l and A denote the length and cross-sectional area of the rectangular pellet.[16, 36]

In the direct current (DC) method, the resistance (R) is obtained from the material's current response (I) to the applied voltage (V), described by R = V/I. In the alternating current (AC) method, the total resistance is achieved from the intercept with the real axis (Z') of the Nyquist plot. The conductivity values from both DC and AC methods were close to each other.

According to our conductivity data at variable temperatures, $LaCa_2Fe_2GaO_8$ exhibits substantially higher conductivity than $La_3Fe_2GaO_9$ ($LaFe_{0.67}Ga_{0.33}O_3$) in the whole temperature range, as shown in Figure 4a. The electrical conductivities of both materials increase as a function of temperature, similar to the typical behavior of semiconductors.[16, 18]

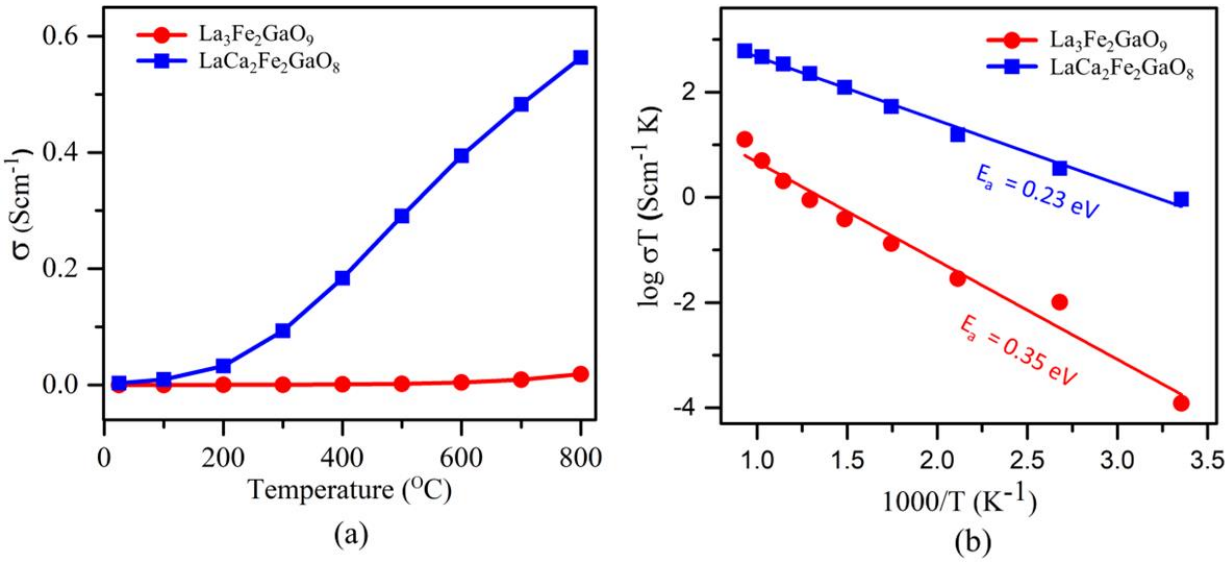

Figure 4. (a) Electrical conductivity as a function of temperature for $La_3Fe_2GaO_9$ ($LaFe_{0.67}Ga_{0.33}O_3$, red) and (b) $LaCa_2Fe_2GaO_8$ (blue). (b) Arrhenius plots to determine the activation energies (E_a) for the temperature-activated increase in conductivity.

The activation energy for the temperature-dependent changes in the conductivity can be obtained by using the Arrhenius equation. [37-39]

$$\sigma T = \sigma^0 e^{-\frac{E_a}{KT}}$$

Where σ° is a pre-exponential factor that is a characteristic of each material. E_a, K, and T are the activation energy for the electrical conductivity, Boltzmann constant, and absolute temperature, respectively. The activation energy (E_a) can be obtained from the slope of the line of best fit in the log σT vs 1000/T plot, as shown in Figure 4b. The activation energy values are consistent with the conductivity trend in the two materials. $LaCa_2Fe_2GaO_8$, which shows higher conductivity, has lower activation energy, compared to $La_3Fe_2GaO_9$ ($LaFe_{0.67}Ga_{0.33}O_3$) which has lower conductivity and higher activation energy.

3.3. Electrocatalytic Activity for Hydrogen Evolution Reaction

Production of Hydrogen via electrochemical water splitting is a sustainable and low emission process as an alternative to natural gas and fossil fuel-based methods. [40-43] In the present study, both materials were examined as electrocatalysts for hydrogen evolution reaction (HER). The vacancy-ordered material $LaCa_2Fe_2GaO_8$ shows superior electrocatalytic performance compared to $La_3Fe_2GaO_9$ ($LaFe_{0.67}Ga_{0.33}O_3$). The HER overpotential (η_{10}) at 10 mA/cm^2 for the latter is 0.62 V, as compared to 0.47 V for the former in 0.5 M H_2SO_4 (Figure 5a). The current density of 10 mA cm^{-2} is the expected current density in a 10% efficient integrated solar-to-fuel system.[40, 44-45] These overpotentials are clearly higher than that of Pt/C (η_{10} = ~0.1 V) which is the state-of-the-art electrocatalyst for HER.[24, 44, 46-47] However, the clear impact of vacancy order on the enhancement of the HER activity is noteworthy. Chronopotentiometry experiments for the best performing material, $LaCa_2Fe_2GaO_8$, show a stable response for at least 10 hours (inset of Figure

5a). Also, X-ray diffraction data before and after the HER experiment (Figure 5c) shows little change, indicating that the material has retained its structural integrity upon the HER process.

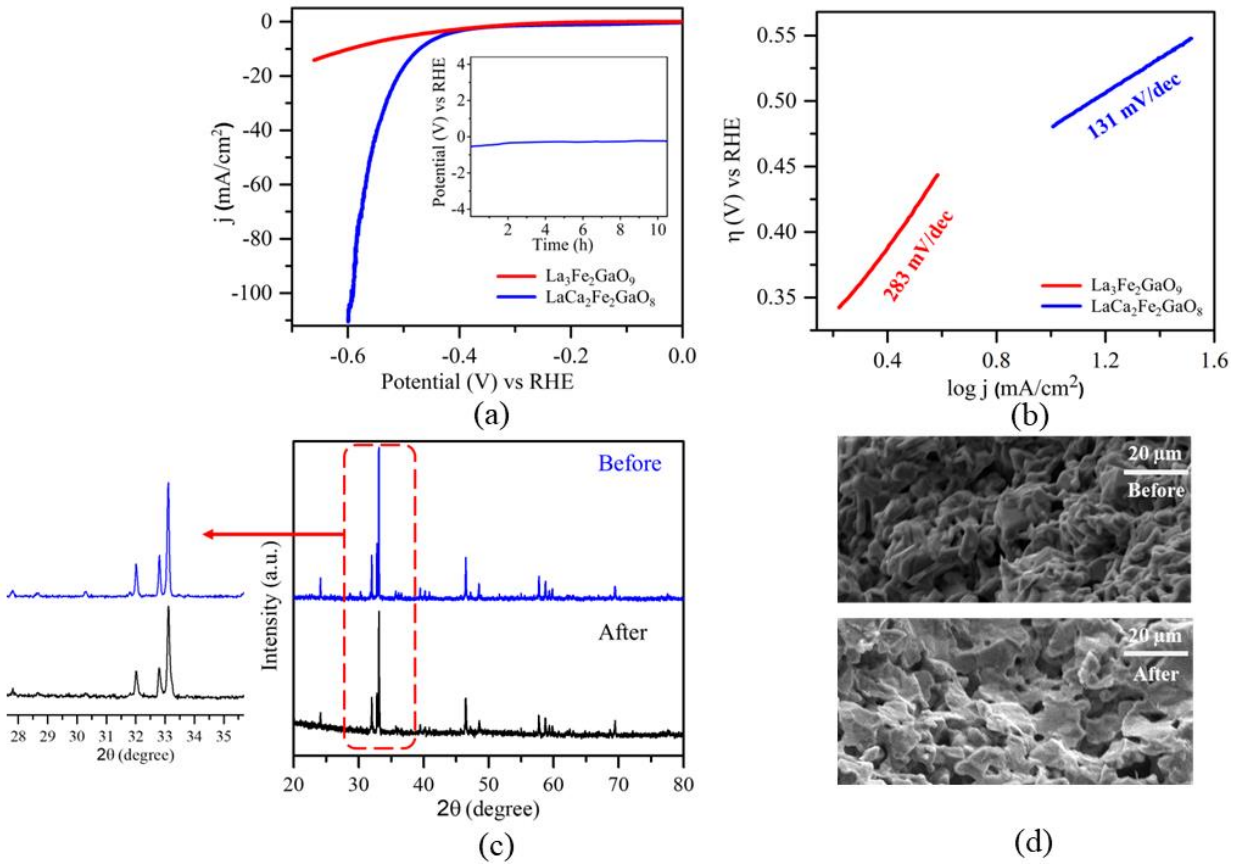

Figure 5. (a) Polarization curves for HER in 0.5 M H_2SO_4. The inset shows chronopotentiometry data for $LaCa_2Fe_2GaO_8$. (b) Tafel plots and slopes. (c) and (d) show X-ray diffraction data and SEM images before and after chronopotentiometry experiments for $LaCa_2Fe_2GaO_8$.

The reaction kinetics was evaluated using the Tafel equation [48-49] $\eta = a + b \log j$, by plotting the overpotential (η) as a function of log j (where j is current density) in Figure 5b. The slope of this plot [44, 50] is indicative of the reaction kinetics. A smaller slope implies a faster reaction since less overpotential is required to start the HER at the same current density increment. [51-53] This is associated with faster electron-transfer kinetics which is consistent with enhanced electrocatalytic

performance. The Tafel slope for $LaCa_2Fe_2GaO_8$ is significantly smaller than that of $La_3Fe_2GaO_9$, as shown in Figure 5b. This trend matches the electrocatalytic activities of these compounds, where a lower Tafel slope belongs to the catalyst with better HER activity. [15, 24, 44, 54]

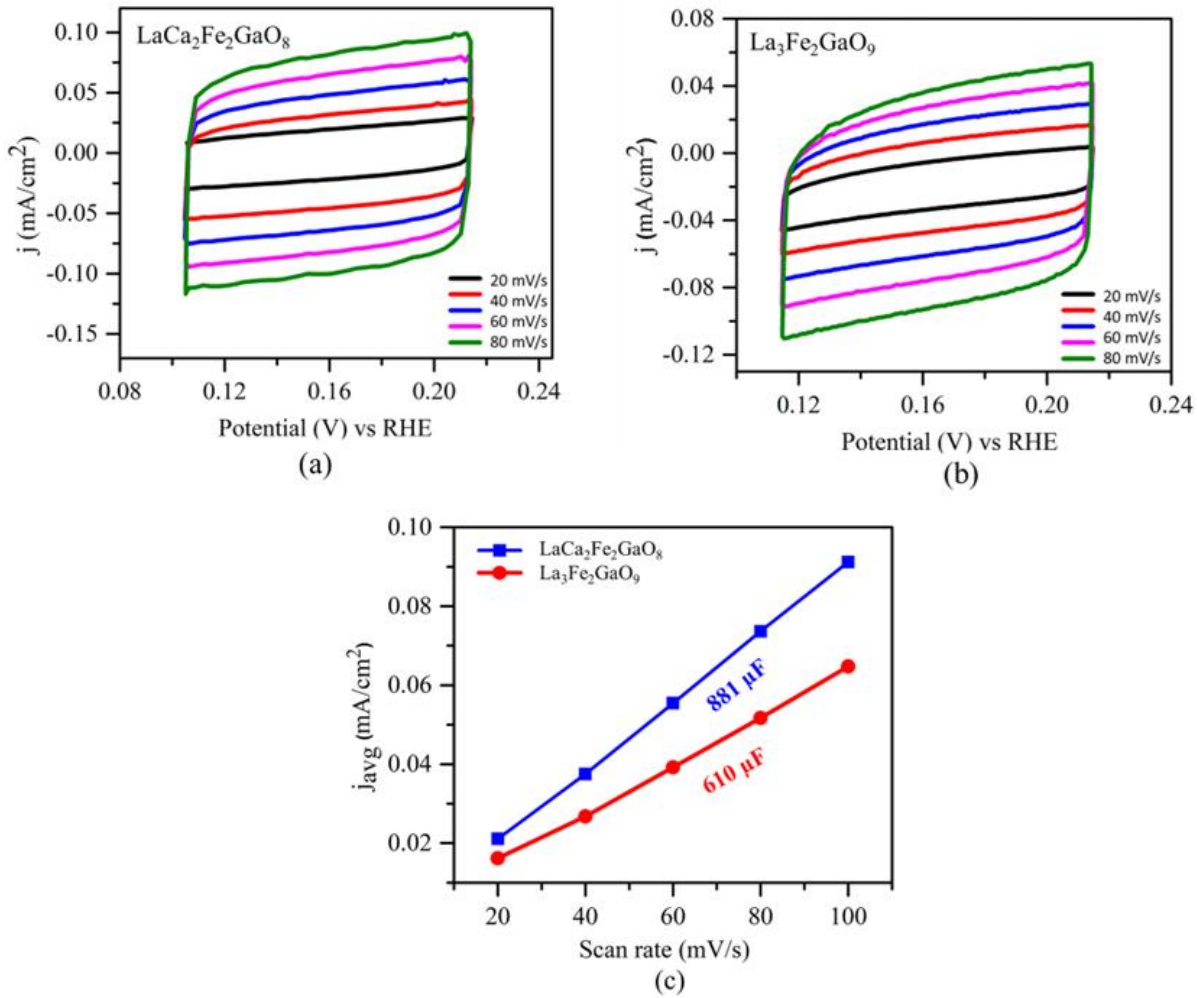

Figure 6. (a) and (b) Cyclic voltammetry (CV) data in non-Faradaic region in 0.5 M H_2SO_4. (c) Plot of $j_{average}$ obtained from the above CVs as a function of scan rate, where the slope is the double layer capacitance.

The Tafel slope denotes the overpotential difference needed to change the current density by 10-fold in the HER process.[44] Therefore, it indicates the rate-determining step in the HER reaction

mechanism.[48] The HER process can happen by either Volmer-Heyrovsky or Volmer-Tafel steps.[53] If the Volmer step becomes the rate-determining step, the Tafel slope should be around 116 mV/dec. When the Heyrovsky step and Tafel step are rate-determining steps, the Tafel slope should be around 39 mV/dec and 29 mV/dec, respectively. [48] Also, there can be different Tafel slope values that indicate more than one rate-determining step. For instance, some perovskite oxides, such as $Ca_2FeMnO_{6-\delta}$, show a larger Tafel slope (178 mV/dec),[24] indicating a mixed HER mechanism in an acidic medium. Also, the larger Tafel slopes in some other catalysts, such as Mo_2C film (Tafel slope 166 mV/dec),[55] and P-doped $NiMoO_4$ (Tafel slope 174 mV/dec)[56] have been assigned to having more than one rate-determining steps in the HER mechanism. Here, the Tafel slope of 131 mV/dec for $LaCa_2Fe_2GaO_8$ is close to that expected for a mechanism where the Volmer step is the rate-determining step. The larger Tafel slope for $La_3Fe_2GaO_9$ (283 mV/dec) can indicate more than one rate-determining step.

We have determined the double-layer capacitance (C_{dl})[24-25, 57] using the average current densities (j_{ave}) at different scan rates, obtained from cyclic voltammograms at non-faradic regions (Figure 6). The slope of the plot of j_{ave} versus v gives the double layer capacitance [25] according to the equation $j_{avg} = C_{dl}\ v$. Some studies have correlated the double layer capacitance with the electrochemically active surface area,[52] which represents the area of the catalyst that is accessible to adsorbates during the reaction.[4] Here, $LaCa_2Fe_2GaO_8$, which is a more active catalyst, also shows a higher value of C_{dl} compared to $La_3Fe_2GaO_9$ ($LaFe_{0.67}Ga_{0.33}O_3$), as shown in Figure 6.

Conclusions

The electrocatalytic activity for HER can be improved by creating an ordered array of oxygen vacancies, as demonstrated by $LaCa_2Fe_2GaO_8$, where oxygen vacancies appear in every third layer

of the structure, converting the octahedral geometry into tetrahedral. The effect of oxygen vacancies is evident when the electrocatalytic performance of this material is compared to that of $La_3Fe_2GaO_9$ ($LaFe_{0.67}Ga_{0.33}O_3$), which has the same Fe/Ga stoichiometry but no oxygen-vacancies, since it contains only La^{3+} on the A-site. Since the catalytically active metals in oxide HER catalysts are transition metals, the role of A-site metal is to modify the concentration of vacancies and the structural features of the materials. The vacancy-ordered oxide $LaCa_2Fe_2GaO_8$ shows a significantly better electrocatalytic performance for HER compared to $La_3Fe_2GaO_9$ ($LaFe_{0.67}Ga_{0.33}O_3$). The former also shows greater electrical conductivity and faster HER kinetics.

Acknowledgment. This work is supported by the National Science Foundation (NSF) under grant no. DMR-1943085.

References

[1] Z. W. Seh, J. Kibsgaard, C. F. Dickens, I. Chorkendorff, J. K. Nørskov, T. F. Jaramillo, *Science* **2017**, *355*.
[2] C. Hu, L. Zhang, J. Gong, *Energy Environ. Sci.* **2019**, *12*, 2620-2645.
[3] X. Zou, Y. Zhang, *Chem. Soc. Rev.* **2015**, *44*, 5148-5180.
[4] S. B. Karki, F. Ramezanipour, *ACS Appl. Energy Mater.* **2020**, *3*, 10983-10992.
[5] M. S. Alom, C. C. Kananke-Gamage, F. Ramezanipour, *ACS omega* **2022**, *7*, 7444-7451.
[6] F. Li, G.-F. Han, H.-J. Noh, J.-P. Jeon, I. Ahmad, S. Chen, C. Yang, Y. Bu, Z. Fu, Y. Lu, *Nat. Commun.* **2019**, *10*, 1-7.
[7] R. Sachse, D. Bernsmeier, R. Schmack, I. Häusler, A. Hertwig, K. Kraffert, J. Nissen, R. Kraehnert, *Catal. Sci. Technol* **2020**, *10*, 2057-2068.
[8] H.-Y. Chen, H.-J. Niu, X. Ma, J.-J. Feng, X. Weng, H. Huang, A.-J. Wang, *J. Colloid Interface Sci.* **2020**, *561*, 372-378.
[9] J. Suntivich, K. J. May, H. A. Gasteiger, J. B. Goodenough, Y. Shao-Horn, *Science* **2011**, *334*, 1383-1385.
[10] W.-J. Yin, B. Weng, J. Ge, Q. Sun, Z. Li, Y. Yan, *Energy Environ. Sci.* **2019**, *12*, 442-462.
[11] J. Kim, X. Yin, K.-C. Tsao, S. Fang, H. Yang, *J. Am. Chem. Soc.* **2014**, *136*, 14646-14649.
[12] M. S. Alom, F. Ramezanipour, *ChemCatChem* **2021**, *13*, 3510-3516.
[13] R. K. Hona, F. Ramezanipour, *Inorg. Chem.* **2020**, *59*, 4685-4692.
[14] Q. Sun, Z. Dai, Z. Zhang, Z. Chen, H. Lin, Y. Gao, D. Chen, *J. Power Sources* **2019**, *427*, 194-200.
[15] S. B. Karki, R. K. Hona, M. Yu, F. Ramezanipour, *ACS Catal.* **2022**, *12*, 10333-10337.
[16] R. K. Hona, A. Huq, F. Ramezanipour, *Inorg. Chem.* **2017**, *56*, 14494-14505.
[17] J. Wang, Y. Gao, D. Chen, J. Liu, Z. Zhang, Z. Shao, F. Ciucci, *ACS Catal.* **2018**, *8*, 364-371.
[18] R. K. Hona, A. Huq, S. Mulmi, F. Ramezanipour, *Inorg. Chem.* **2017**, *56*, 9716-9724.
[19] J.-C. Grenier, J. Darriet, M. Pouchard, P. Hagenmuller, *Mater. Res. Bull.* **1976**, *11*, 1219-1225.
[20] P. D. Battle, S. J. Blundell, P. Santhosh, M. J. Rosseinsky, C. Steer, *J. Condens. Matter Phys.* **2002**, *14*, 13569.
[21] P. Battle, T. Gibb, P. Lightfoot, *J. Solid State Chem.* **1990**, *84*, 237-244.
[22] K. Luo, M. A. Hayward, *J. Solid State Chem.* **2013**, *198*, 203-209.
[23] J. Hudspeth, D. Goossens, A. J. Studer, R. Withers, L. Norén, *J. Condens. Matter Phys.* **2009**, *21*, 124206.
[24] R. K. Hona, S. B. Karki, F. Ramezanipour, *ACS Sustain. Chem. Eng.* **2020**, *8*, 11549-11557.
[25] R. K. Hona, F. Ramezanipour, *Angew Chem.* **2019**, *131*, 2082-2085.
[26] S. B. Karki, R. K. Hona, F. Ramezanipour, *Ionics* **2022**, *28*, 397-406.
[27] A. C. Larson, R. B. Von Dreele, *Los Alamos, New Mexico: Los Alamos National Laboratory* **2004**.
[28] B. H. Toby, *J. Appl. Crystallogr.* **2001**, *34*, 210-213.
[29] R. K. Hona, F. Ramezanipour, *J. Mater. Sci. Mater. Electron* **2018**, *29*, 13464-13473.
[30] K. Huang, H. Y. Lee, J. B. Goodenough, *J. Electrochem. Soc.* **1998**, *145*, 3220.
[31] Y. Zhu, W. Zhou, J. Yu, Y. Chen, M. Liu, Z. Shao, *Chem. Mater.* **2016**, *28*, 1691-1697.
[32] T. Ishihara, H. Matsuda, Y. Takita, *J. Am. Chem. Soc.* **1994**, *116*, 3801-3803.
[33] C. C. Kananke-Gamage, F. Ramezanipour, *Dalton Trans.* **2021**, *50*, 14196-14206.
[34] X. Cheng, E. Fabbri, M. Nachtegaal, I. E. Castelli, M. El Kazzi, R. Haumont, N. Marzari, T. J. Schmidt, *Chem. Mater.* **2015**, *27*, 7662-7672.
[35] M.-J. Choi, T. L. Kim, J. K. Kim, T. H. Lee, S. A. Lee, C. Kim, K. Hong, C. W. Bark, K.-T. Ko, H. W. Jang, *Nano Lett.* **2020**, *20*, 8040-8045.
[36] Y. Singh, in *Int. J. Mod. Phys. Conf. Ser., Vol. 22*, World Scientific, **2013**, pp. 745-756.
[37] L. Sudha, R. Sukumar, K. Uma Rao, *International Journal of Materials. Mechanics and Manufacturing* **2014**, *2*, 96-100.

[38] S. Pizzini, *Physical chemistry of semiconductor materials and processes*, John Wiley & Sons, **2015**.
[39] R. Andoulsi, K. Horchani-Naifer, M. Ferid, *Ceram. Int.* **2013**, *39*, 6527-6531.
[40] H. Park, I. J. Park, M. G. Lee, K. C. Kwon, S.-P. Hong, D. H. Kim, S. A. Lee, T. H. Lee, C. Kim, C. W. Moon, *ACS Appl. Mater. Interfaces.* **2019**, *11*, 33835-33843.
[41] A. K. Nayak, M. Verma, Y. Sohn, P. A. Deshpande, D. Pradhan, *ACS omega* **2017**, *2*, 7039-7047.
[42] A. Galal, N. F. Atta, S. M. Ali, *Electrochim. Acta* **2011**, *56*, 5722-5730.
[43] J. D. Benck, T. R. Hellstern, J. Kibsgaard, P. Chakthranont, T. F. Jaramillo, *ACS Catal.* **2014**, *4*, 3957-3971.
[44] J. Zhu, L. Hu, P. Zhao, L. Y. S. Lee, K.-Y. Wong, *Chem. Rev.* **2019**, *120*, 851-918.
[45] C. C. McCrory, S. Jung, I. M. Ferrer, S. M. Chatman, J. C. Peters, T. F. Jaramillo, *J. Am. Chem. Soc.* **2015**, *137*, 4347-4357.
[46] J. Greeley, T. F. Jaramillo, J. Bonde, I. Chorkendorff, J. K. Nørskov, *Nat. Mater.* **2006**, *5*, 909-913.
[47] X. Xu, Y. Chen, W. Zhou, Z. Zhu, C. Su, M. Liu, Z. Shao, *Adv. Mater. Interfaces* **2016**, *28*, 6442-6448.
[48] A. P. Murthy, J. Theerthagiri, J. Madhavan, *J. Phys. Chem. C* **2018**, *122*, 23943-23949.
[49] Z. Peng, K. Wang, W. Xu, B. Wang, B. Mao, Y. Han, C.-K. Tsung, B. Yang, Z. Liu, Y. Li, *ACS Appl. Energy Mater.* **2020**, *3*, 5219-5228.
[50] C. Ling, Y. Ouyang, L. Shi, S. Yuan, Q. Chen, J. Wang, *ACS Catal.* **2017**, *7*, 5097-5102.
[51] S. Oh, H. Kim, Y. Kwon, M. Kim, E. Cho, H. Kwon, *J. Mater. Chem. A* . **2016**, *4*, 18272-18277.
[52] Y. Pan, Y. Chen, X. Li, Y. Liu, C. Liu, *RSC Adv.* **2015**, *5*, 104740-104749.
[53] T. Shinagawa, A. T. Garcia-Esparza, K. Takanabe, *Sci. Rep.* **2015**, *5*, 1-21.
[54] Y. Bu, H. Jang, O. Gwon, S. H. Kim, S. H. Joo, G. Nam, S. Kim, Y. Qin, Q. Zhong, S. K. Kwak, *J. Mater. Chem. A* . **2019**, *7*, 2048-2054.
[55] S. Chaitoglou, T. Giannakopoulou, T. Speliotis, A. Vavouliotis, C. Trapalis, A. Dimoulas, *Nanotechnology* **2019**, *30*, 125401.
[56] W. Xi, G. Yan, H. Tan, L. Xiao, S. Cheng, S. U. Khan, Y. Wang, Y. Li, *Dalton Trans.* **2018**, *47*, 8787-8793.
[57] B. Konkena, I. Sinev, S. Piontek, O. Khavryuchenko, J. P. Dürholt, R. Schmid, H. Tüysüz, M. Muhler, W. Schuhmann, U.-P. Apfel, *Nat. Commun.* **2016**, *7*, 1-8.

Table of Contents Graphic

The presence of an ordered array of oxygen vacancies in $LaCa_2Fe_2GaO_8$ leads to a significant improvement of the electrocatalytic properties for hydrogen-evolution reaction, as compared to $La_3Fe_2GaO_9$ ($LaFe_{0.67}Ga_{0.33}O_3$), which lacks oxygen-vacancies.